Electronic Supplementary Information

Experimental Section

Materials

Graphene oxide (GO) powder and activated carbon (AC) were supplied by Chengdu TIMESNANO. Nickel foam (NF, 1.7 mm) was purchased from Taiyuan Lizhiyuan battery material Co., LTD., China. Cobalt nitrate hexahydrate ($Co(NO_3)_2 \cdot 6H_2O$, 98.5%), 2-methylimidazole (2-MIM, 99%), thioacetamide (TAA, 99%), sodium borohydride ($NaBH_4$, 98%), sodium hydroxide (99%), ascorbic acid (98%), methanol (99.9%) and ethanol (99.9%) were obtained from Aladdin Co., Ltd. All Chemicals and reagents were of analytical grade and used without further purification.

Preparation of the rGO/NF

In a typical synthesis, 0.01 g GO powders were dispersed in 40 mL deionized water under stirring overnight followed by sonication for 1 h to form a homogeneous brown suspension. Then, 0.1g ascorbic acid was added. After stirring for 30 min, a piece of clean NF was immersed into the suspension, and the suspension was heated at 80 ^oC for 6 h in a water bath. Finally, the rGO/NF was taken out, cleaned with deionized water and ethanol, and dried at 60 ^oC overnight.

Preparation of the Co-ZIL-L nanosheet arrays on rGO/NF

1.313 g 2-MIM and 0.582 g Co $(NO_3)_2 \cdot 6H_2O$ were dissolved in 40 mL deionized water. Then, a piece of rGO/NF was placed into the above solution, and the mixture was stirred for 10 min. After that, the solution was left static for 4h at ambient

condition. Finally, the Co-ZIF-L/rGO/NF was cleaned with deionized water and ethanol, and dried at 60 ^{o}C overnight.

Preparation of the Co_3S_4/rGO/NF

The Co-ZIL-L/rGO/NF was immersed into an ethanol solution (40 mL) of TAA (0.120 g) in a Teflon-lined autoclave. The autoclave was heated in a 120 ^{o}C oven for 4 h. After cooling to room temperature, the Co_3S_4/rGO/NF was taken out, washed and dried.

Preparation of the V_S-Co_3S_4/rGO/NF

1.513 g $NaBH_4$ was dissolved in 80 mL deionized water. Then, the Co_3S_4/rGO/NF was immersed into the solution for 2 h at ambient temperature. The product was washed with deionized water and ethanol for several times, and then dried overnight. The mass loading of V_S-Co_3S_4 on rGO/NF was around 2.4 mg cm^{-2}.

Characterization

The electrode materials were characterized by X-ray photoelectron spectrometer (XPS, Thermo Fisher Scientific ESCALAB 250Xi), X-ray diffractometer (XRD, Bruker AXS D8 Advance), electron paramagnetic resonance (EPR), field emission scanning electron microscope (FESEM, Hitachi S-4800) and transmission electron microscope (TEM, FEI Talos F200x) equipped with energy dispersive X-ray spectroscopy (EDS). N_2 physisorption measurements were carried out at 77 K using a Micromeritics ASAP 2040 analyzer. The electrical conductivity was measured by 4-probe conductivity measurements on ST-2722 semiconductor resistivity tester. UV-

visible absorption spectra were recorded by a spectrophotometer (PerkinElmer Lambda 35).

Electrochemical measurements

The electrochemical properties of the V_S-Co_3S_4/rGO/NF and Co_3S_4/rGO/NF electrode were investigated by a cell with three-electrode configuration using Pt foil as counter electrode and saturated calomel electrode (SCE) as reference electrode in 2.0 M KOH aqueous solution. All the tests including galvanostatic charge-discharge (GCD), electrochemical impedance spectroscopy (EIS) and cyclic voltammetry (CV) were carried out on a CHI 660E electrochemical workstation (Shanghai Chenhua). The specific capacitance (C_s, F g^{-1}) of the electrode material was calculated by following equation:

$$C_s = \frac{I \times \Delta t}{m \times \Delta V} \quad \text{(S1)}$$

where I (A), Δt (s), ΔV (V) and m (g) were the discharging current, discharging time, potential window for the charge-discharge process and mass loading of active materials, respectively.

A two-electrode cell was assembled by using the V_S-Co_3S_4/rGO/NF as positive electrode and an activated carbon (AC) as negative electrode in 2.0 M KOH. The mass loading of active materials on both electrodes was optimized to achieve charge (Q) balance, as described in following equation:

$$Q_- = m_- \times C_- \times \Delta V_- = m_+ \times C_+ \times \Delta V_+ = Q_+ \quad \text{(S2)}$$

where m (g), C (F g^{-1}) and ΔV (V) represented the mass of active materials, specific capacitance, and charge-discharge potential window of both electrodes, respectively.

The energy density (E, Wh kg^{-1}) and power density (W kg^{-1}) of the V_S-Co_3S_4/rGO//AC cell were calculated as follows:

$$E = \frac{C_s \times (\Delta V)^2}{2 \times 3.6} \quad \text{(S3)}$$

$$P = \frac{3600 \times E}{\Delta t} \quad \text{(S4)}$$

where C_s (F g^{-1}), ΔV (V) and Δt (s) represented specific capacitance, working voltage window and discharging time of the V_S-Co_3S_4/rGO//AC cell, respectively.

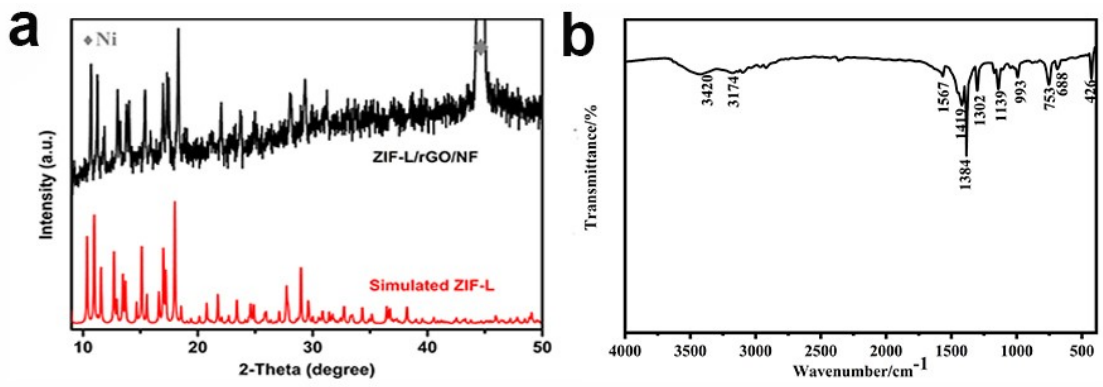

Fig. S1. (a) XRD pattern of ZIF-L/rGO/NF and FTIR spectrum of ZIF-L.

As shown in Fig. S1a, the XRD pattern of Co-ZIF is match well with that of simulated ZIF-L, indicating the successful synthesis of ZIF-L. The FTIR spectrum of ZIF-L scratched from the NF is shown in Fig. S1b. It shows main absorptions at 426 cm^{-1} (Co–N stretching), 688 and 753 cm^{-1} (out-of-plane bending of the imidazole ring), 993 cm^{-1} (C–N stretching), 1139 and 1302 cm^{-1} (C–H vibration), 1384 and 1419 cm^{-1} (C–C stretching), and 1567 cm^{-1} (C=N stretching), which is consistent with previous reports.[1]

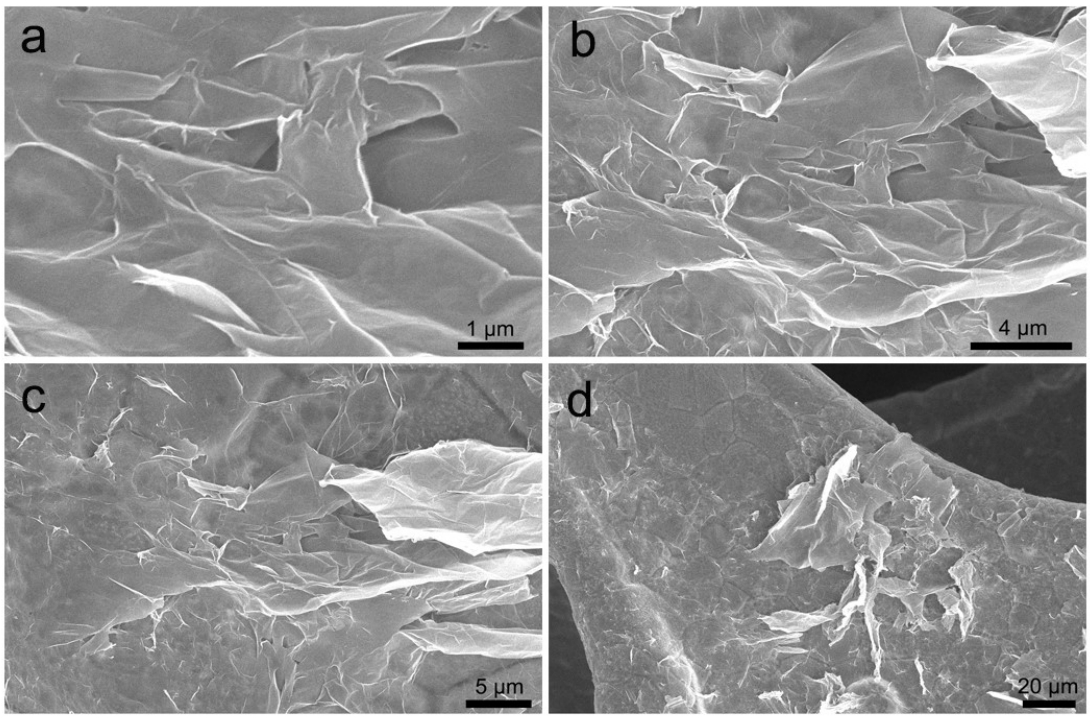

Fig. S2. SEM images of rGO/NF.

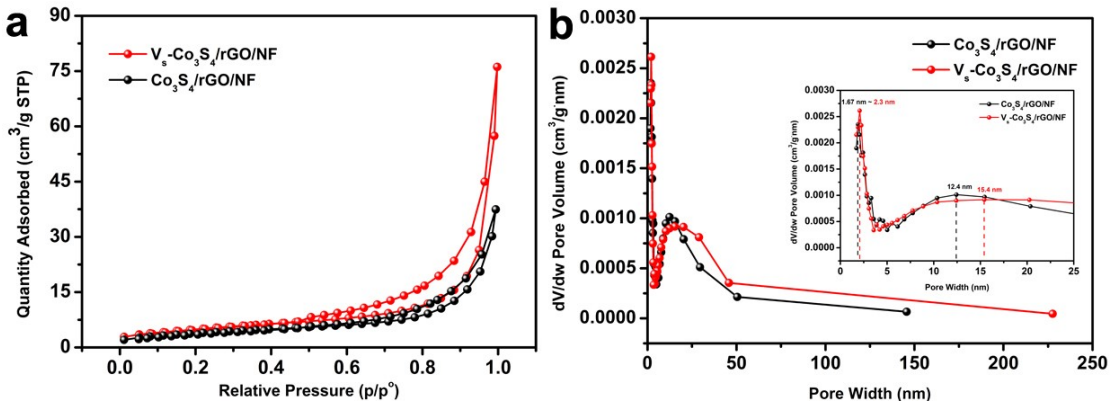

Fig. S3. (a) Nitrogen physisorption isotherms and the corresponding pore size distributions of Co_3S_4 and V_S-Co_3S_4.

The samples display the typical IV isotherm with H3 type hysteresis (Fig. S4a), implying that the sample contains mesopores. The specific surface area of V_S-Co_3S_4 (18.2 m^2 g^{-1}) is larger than that of Co_3S_4 (14.1 m^2 g^{-1}). The pore size distribution (Fig. S4b) shows that there are two main mesopores at ~2 and 15 nm, respectively. Such hierarchical porous structure is conducive to the acquisition of electrolyte, and the large specific surface area will expose more electroactive sites, which is conducive to faradaic redox reactions.

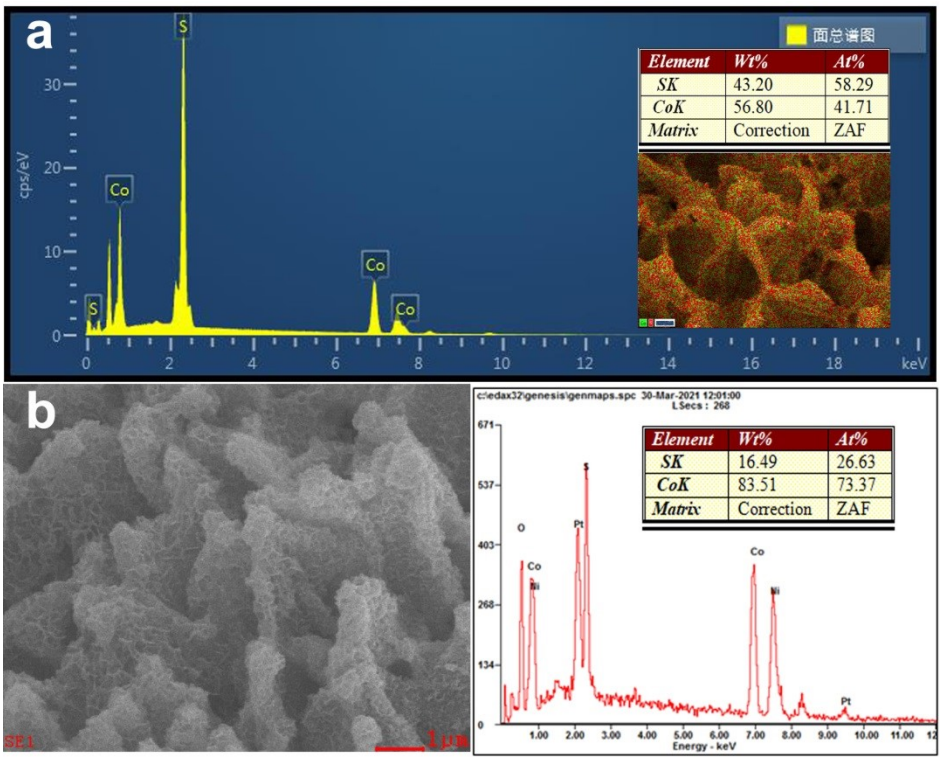

Fig. S4. EDS patterns of the (a) Co_3S_4/rGO/NF and (b) V_S-Co_3S_4/rGO/NF.

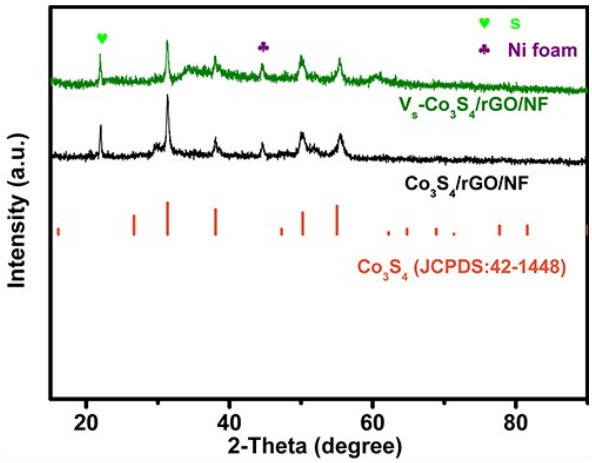

Fig. S5 XRD patterns of V_S-Co_3S_4/rGO/NF and Co_3S_4/rGO/NF.

X-ray diffraction (XRD) was used to determine the crystalline phases of V_S-Co_3S_4/rGO/NF and Co_3S_4/rGO/NF. In attempt to avoid the interference of NF, the samples were scratched from the substrate. As shown in Fig. S3, both samples display peaks at 31.4, 38.0, 50.2 and 55.0° corresponding to the (311), (400), (511), (440) planes of the cubic Co_3S_4 (JCPDS No. 42-1448). Besides, the additional peak at 22° is attributed to to S (JCPDS No. 24-1251) caused by decomposition of TAA.

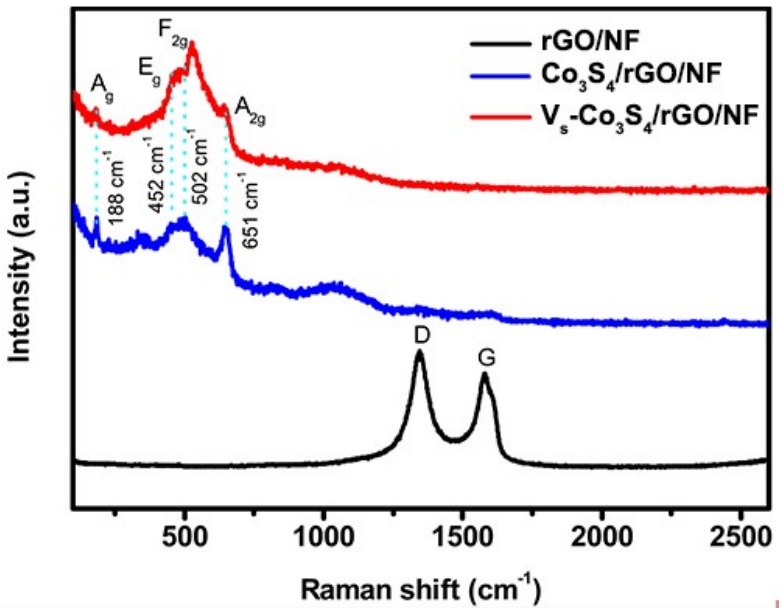

Fig. S6 Raman spectra of rGO/NF, Co_3S_4/rGO/NF and V_S-Co_3S_4/rGO/NF.

Raman measurements were conducted to obtain more information on the structure of the sample. The Raman spectra of the samples are shown in Fig. S4. rGO/NF has two obvious peaks at 1345 and 1596 cm^{-1}, corresponding to the D and G bands. The peak intensity ratio of the D and G bands (I_D/I_G) can be used to measure the degree of disorder of carbon materials. During the removal of oxygen-containing functional groups of GO in the reduction process, the regular crystalline pattern in the graphene sheet (sp^2 carbon) is destroyed, resulting in an increment in the I_D/I_G value.[2] As shown in the Fig. S5, the I_D/I_G value of rGO/NF (1.32) is higher than that of thermally reduced GO (~0.91) and chemically reduced GO (~0.96),[3] indicating a higher degree of reduction. The apparent peak at 651 cm^{-1} is the characteristic band of cubic Co_3S_4. The decrease of peak strength at 651 cm^{-1} of V_S-Co_3S_4/rGO/NF indicates that sulfur vacancies have been formed. Other active modes, such as E_{2g} and F_g are attributed to metal sulfur bonds which are found toward lower frequencies.[4]

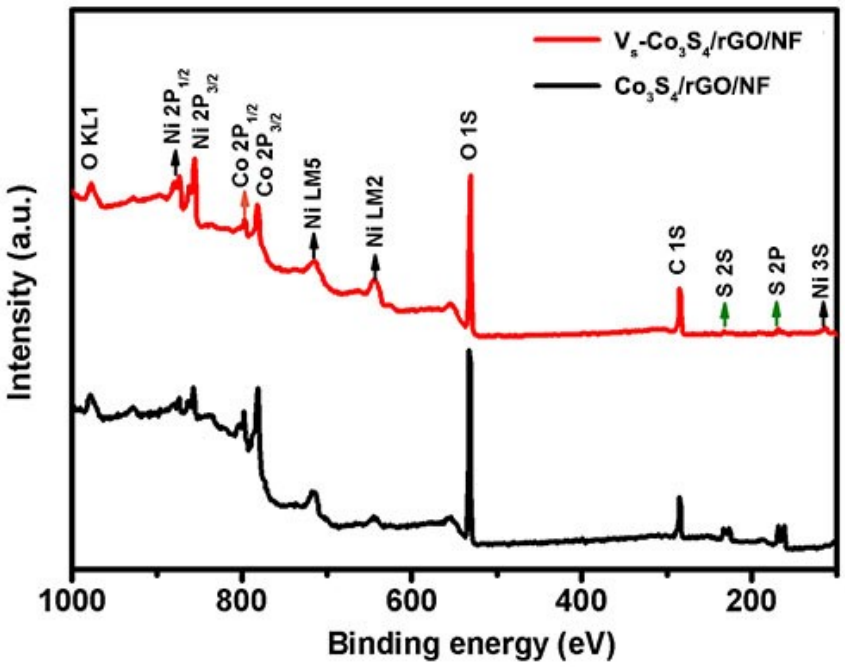

Fig. S7 XPS survey spectra of Co_3S_4/rGO/NF and V_S-Co_3S_4/rGO/NF.

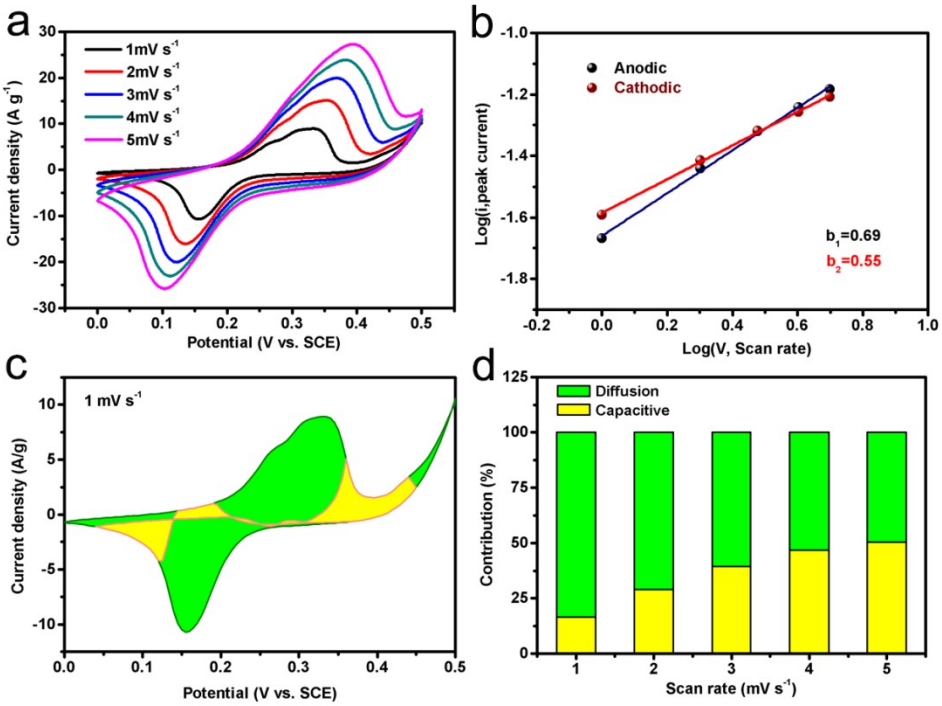

Fig. S8 (a) CV curves, (b) plots of log(*i*) *vs.* log(*υ*), (c) the capacitance contributions of capacitive process and diffusion-controlled processes at 1 mV s^{-1} and (d) the relative contributions of capacitive process and diffusion-controlled process as a function of scan rates of V_S-Co_3S_4/rGO/NF.

The charge storage mechanism of the electrode can be analyzing the relationship between peak current (*i*) and scan rate (*υ*) according to following equation:

$$i=a\upsilon^b \qquad \text{(S5)}$$

where a and b are constants. If b-value equals 0.5, charge storage is diffusion-controlled, while b=1 manifests capacitive process.[5] By the linear fitting log(*i*) vs log(*υ*), the b-values are estimated to be 0.69 and 0.55 for anodic and cathodic process (Fig. S6b), indicating that the charge storage is mainly diffusion-controlled. Meanwhile, the current response can be divided into capacitive ($k_1\upsilon$) and diffusion-controlled ($k_2\upsilon^{1/2}$) parts as follows:

$$i(V) = k_1 \upsilon + k_2 \upsilon^{1/2} \quad \text{(S6)}$$

where k_1 and k_2 are two constants. The fitting (i(V)/υ *vs.* $\upsilon^{1/2}$) at a given potential (V) determines the values of k_1 and k_2. The separation between capacitive and diffusion-controlled processes at a scan rate of 1 mV s^{-1} is shown in Fig. S6c. As the scan rate rises from 1 to 5 mV s^{-1}, the relative contribution fraction of diffusion-controlled process decreases from 83.5 to 49.5% (Fig. S6d), indicating that diffusion-controlled process governs the charge storage.

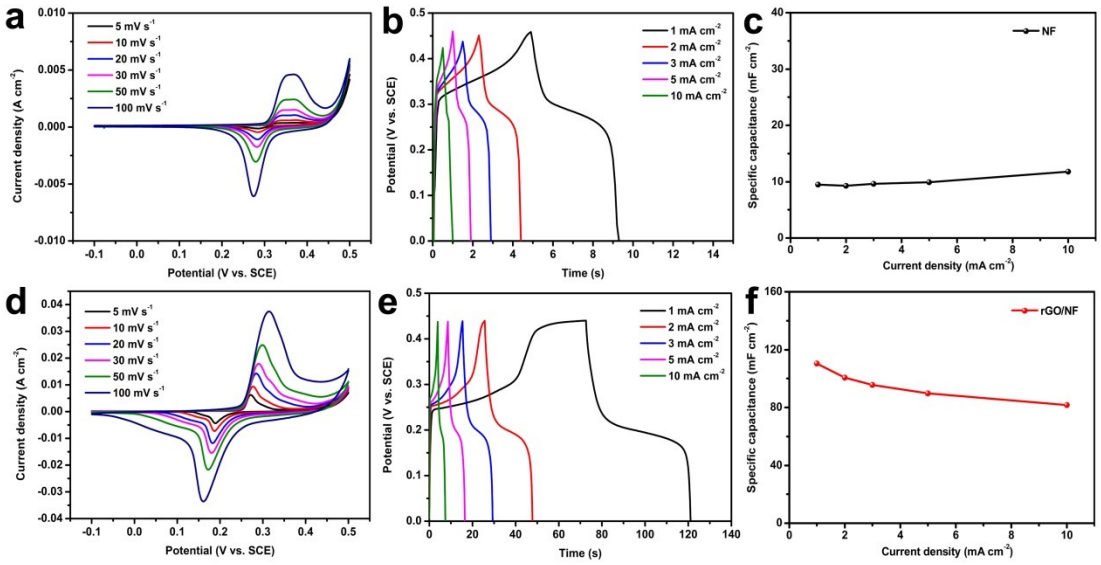

Fig. S9. Electrochemical properties of (a-c) NF and (d-f)rGO/NF. (a, d) CV curves, (b, e) GCD curves and (c, f) specific capacitances at various current densities.

The electrochemical properties of NF and rGO/NF are provided in Fig. S9. At the current density of 1 mA cm^{-2}, the NF and rGO/NF present very low capacitances of 9.5 and 110.5 mF cm^{-2}, respectively. Thus, the contributions of NF and rGO are negligible

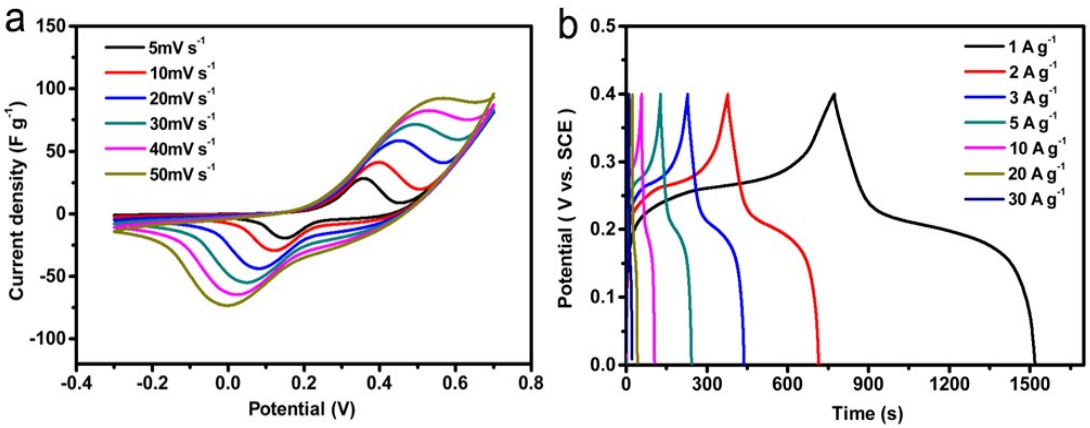

Fig. S10. (a) CV curves of Co_3S_4/rGO/NF at a scan rate of 5-50 mV s^{-1}. (b) GCD curve of Co_3S_4/rGO/NF at a current density of 1-30 A g^{-1}.

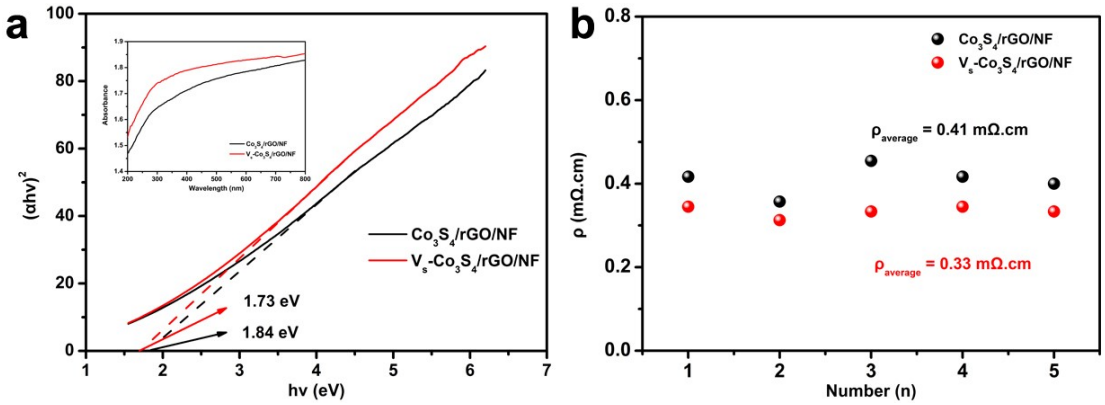

Fig. S11. (a) Plots of $(\alpha hv)^2$ *vs. hv* and UV–vis adsorption spectra (inset), and (b) resistivity at five different points of Co_3S_4/rGO/NF and V_S-Co_3S_4/rGO/NF.

The UV−vis diffuse reflectance spectra (Fig. S11a) are collected and the band gap energy (E_g) is calculated as follows:[6]

$(\alpha hv)^n = K(hv - E_g)$ (S7)

where *hv*is the photoenergy, α is the absorption coefficient, K is a constant relative to the material, and n is either 2 for a direct transition or 1/2 for an indirect transition. The Vs-Co_3S_4/rGO/NF (E_g=1.73 eV) shows lower E_g value than that of Co_3S_4/rGO/NF (E_g=1.84 eV), implying the higher electronic conductivity of Vs-Co_3S_4/rGO/NF.

4-probe conductivity measurements are also conducted, and the resistivity values at five different points are collected, as show in Fig. S11b. The average resistivity value of V_S-Co_3S_4/rGO/NF (0.33 mΩ cm) is lower than that of Co_3S_4/rGO/NF (0.41 mΩ.cm), further confirming the higher electronic conductivity of V_S-Co_3S_4/rGO/NF.

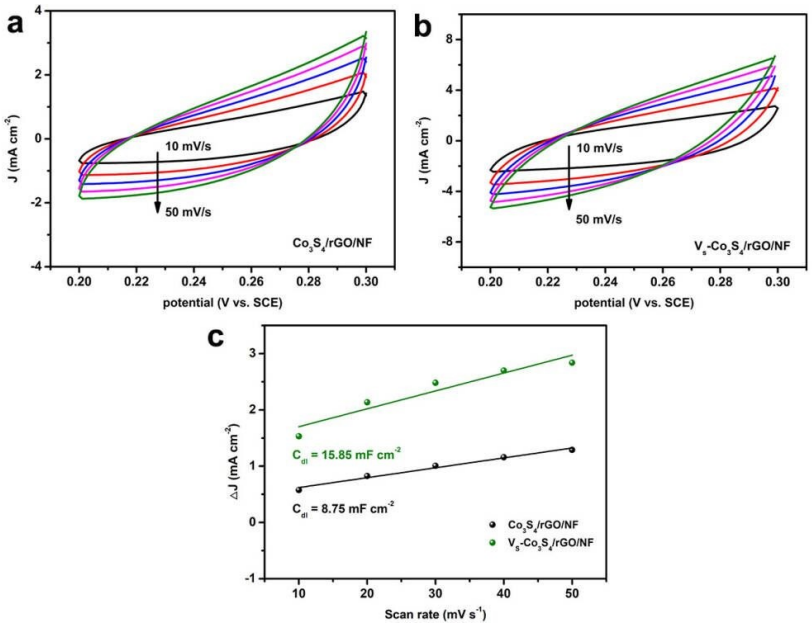

Fig. S12. (a) CV curves of Co_3S_4/rGO/NF. (b) CV curves of V_S-Co_3S_4/rGO/NF. (c) The relationship between charging current density difference and scan rates.

The electrochemical active surface area (ECSA) of the electrode materials is evaluated by the double-layer capacitance (C_{dl}) method as follows:[7]

$ECSA = C_{dl}/C_s$

where C_{dl} and C_s refer to double layer capacitance and midpoint specific capacitance. The C_{dl} is measured in non-faradaic potential window (Fig. S12). As shown in Fig. 12c, the C_{dl} value of the V_S-Co_3S_4/rGO/NF is 15.85 mF cm^{-2}, which is much larger than that of Co_3S_4/rGO/NF (8.753 mF cm^{-2}), revealing that the $NaBH_4$ treatment can result in enriched electrochemical active sites, which is consistent with the N_2 sorption results.

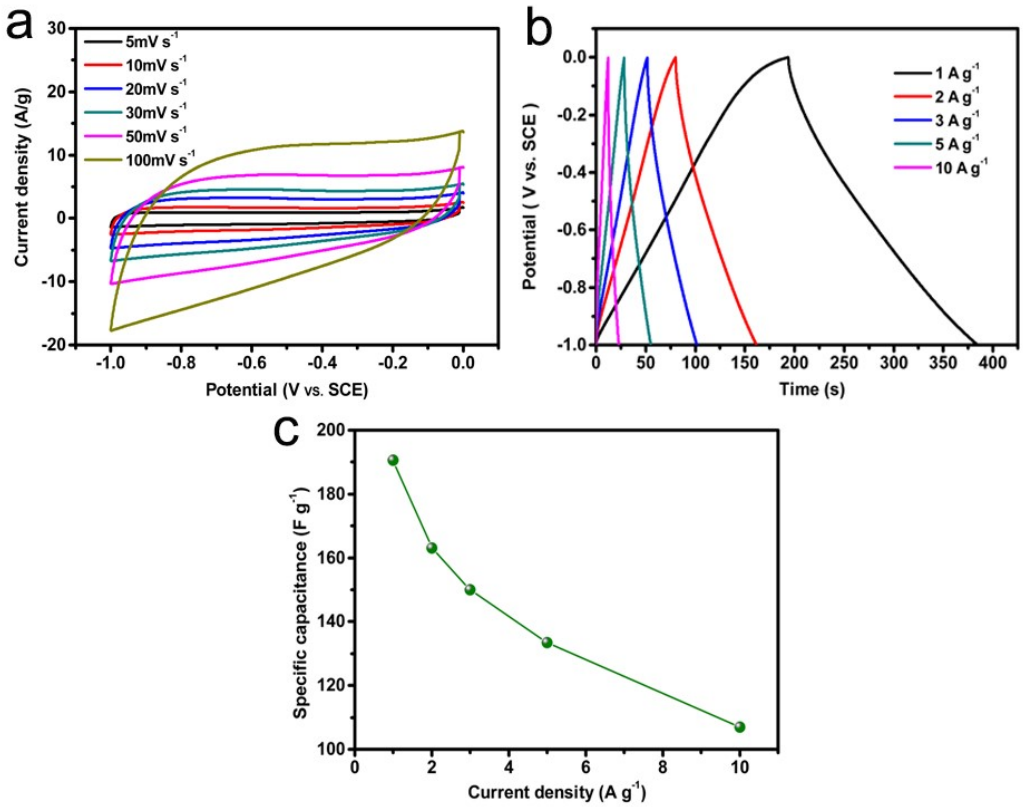

Fig. S13. (a) CV curves of AC at a scan rate of 5-100 mV s^{-1}. (b) GCD curve of AC at a current density of 1-10 A g^{-1}. (c) Specific capacitances of AC at different current densities.

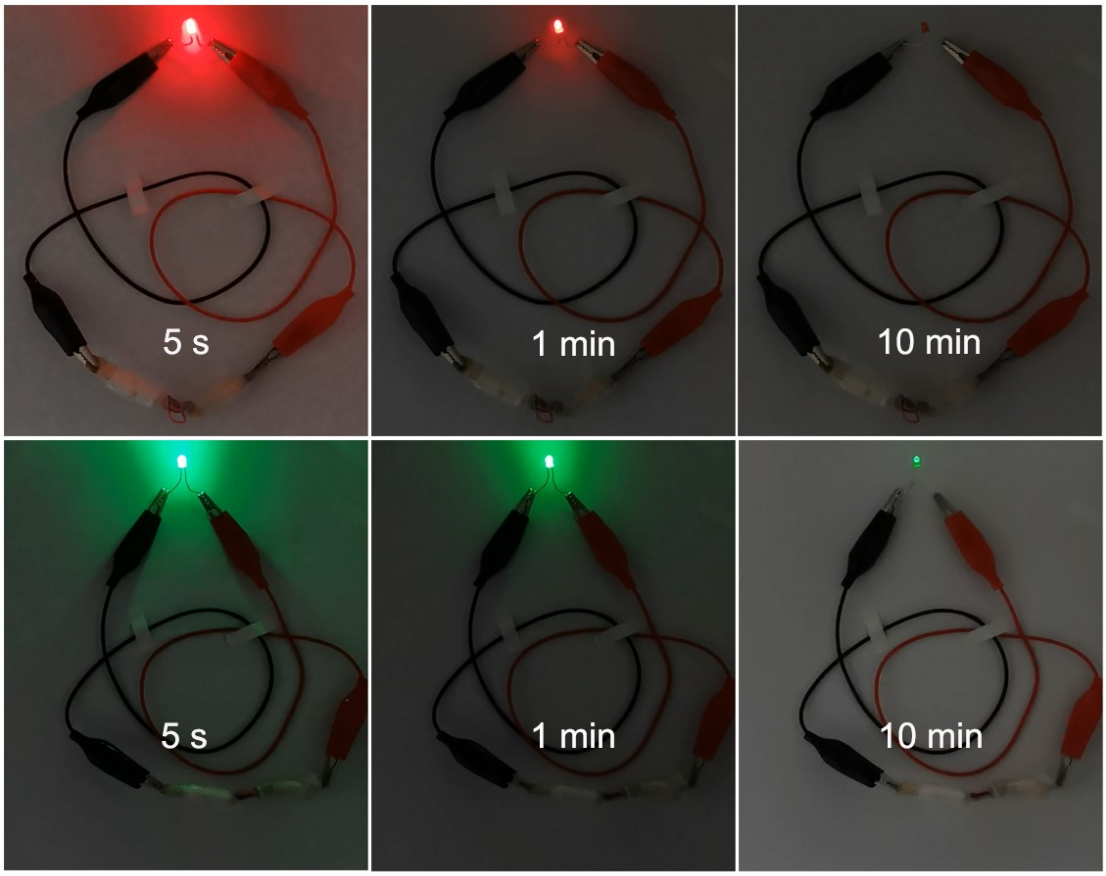

Fig. S14. Photographs of the lighted red and green LEDs powered by two assembled V_S-Co_3S_4/rGO//AC ASCs.

Table S1 Comparison of V_S-Co_3S_4/rGO/NF and reported Co_3S_4-based electrode materials.

Electrode materials	Current density	Specific capacitance	Reference
2D Cobalt sulfide/Graphene	1 A g^{-1}	320 F g^{-1}	[8]
O-$(NiCo)_9S_8$/N, S-doped G	0.5 A g^{-1}	1247 F g^{-1}	[9]
r-$CoNi_2S_4$	1 A g^{-1}	1918.9 F g^{-1}	[10]
rGO-CNT-Co_3S_4	1 A g^{-1}	977 F g^{-1}	[11]
PANI/rGO-Co_3S_4	1 A g^{-1}	767 F g^{-1}	[12]
Co_3S_4/rGO	0.5 A g^{-1}	675.9 F g^{-1}	[13]
Ni–Co–S/G	1 A g^{-1}	1492 F g^{-1}	[14]
Co_3S_4-HNCs@PPy	1 A g^{-1}	1706 F g^{-1}	[15]
V_S-Co_3S_4/rGO/NF	**1 A g^{-1}**	**2615 F g^{-1}**	**this work**

Table S2 The energy density and power density of representative metal sulfide-based ASC devices.

ASC	Energy density	Power density	Reference
Co_9S_8-NSA//AC	20 Wh kg^{-1}	828 W kg^{-1}	[1]
Ni-Co-S//AC	24.8 Wh kg^{-1}	849 W kg^{-1}	[16]
$MnCo_2S_4$//rGO	31.3 Wh kg^{-1}	800 W kg^{-1}	[17]
Ni_3S_2/NiS@Ni_3S_4//rGO	37.7 Wh kg^{-1}	801 W kg^{-1}	[18]
Co_3S_4@$NiCo_2O_4$/rGO//AC	35.7 Wh kg^{-1}	799.3 W kg^{-1}	[19]
O-Co_3S_4/CP//AC	21.3 Wh kg^{-1}	750 W kg^{-1}	[20]
Co_3S_4/PANI//AC	40.75 Wh kg^{-1}	800 W kg^{-1}	[21]
$NiCo_2S_4$/Co_9S_8//AC	36.7 Wh kg^{-1}	800 W kg^{-1}	[22]
Fe-Co-S/NF//rGO	43.6 Wh kg^{-1}	770 W kg^{-1}	[23]
Co_9S_8@C//AC	40 Wh kg^{-1}	850 W kg^{-1}	[24]
V_S-Co_3S_4/rGO//AC	**43.8 Wh kg^{-1}**	**850 W kg^{-1}**	This work

References

1. X. Han, K. Tao, D. Wang and L. Han, *Nanoscale*, 2018, **10**, 2735-2741.
2. S. Li, M. Wang and Y. Lian, *Sci. China Chem.*, 2016, **59**, 405-411.
3. X. Cai, X. Shen, L. Ma, Z. Ji, C. Xu and A. Yuan, *Chem. Eng. J.*, 2015, **268**, 251-259.
4. M. Chauhan and S. Deka, *ACS Appl. Energy Mater.*, 2020, **3**, 977-986.
5. H.-S. Kim, J. B. Cook, H. Lin, Jesse S. Ko, Sarah H. Tolbert, V. Ozolins and B. Dunn, *Nat. Mater.*, 2017, **16**, 454-460.
6. H. Chen, J. Jiang, L. Zhang, H. Wan, T. Qi and D. Xia, *Nanoscale*, 2013, **5**, 8879-8883.
7. X. Yang, X. Sun, L.-Y. Gan, L. Sun, H. Mi, P. Zhang, X. Ren and Y. Li, *J. Mater. Chem. A*, 2020, **8**, 15140-15147.
8. M. Wang, J. Yang, S. Liu, C. Hu, S. Li and J. Qiu, *ACS Appl. Mater. Interfaces*, 2019, **11**, 26235-26242.
9. M. Wang, J. Yang, S. Liu, C. Hu and J. Qiu, *ACS Appl. Energy Mater.*, 2020, **3**, 6977-6984.
10. Y. Liu, Y. Wen, Y. Zhang, X. Wu, H. Li, H. Chen, J. Huang, G. Liu and S. Peng, *Sci. China Mater.*, 2020, **63**, 1216-1226.
11. A. Mohammadi, N. Arsalani, A. G. Tabrizi, S. E. Moosavifard, Z. Naqshbandi and L. S. Ghadimi, *Chem. Eng. J.*, 2018, **334**, 66-80.
12. A. G. Tabrizi, N. Arsalani, Z. Naghshbandi, L. S. Ghadimi and A. Mohammadi, *Int. J. Hydrogen Energy*, 2018, **43**, 12200-12210.
13. Q. Wang, L. Jiao, H. Du, Y. Si, Y. Wang and H. Yuan, *J. Mater. Chem.*, 2012, **22**, 21387-21391.
14. J. Yang, C. Yu, X. Fan, S. Liang, S. Li, H. Huang, Z. Ling, C. Hao and J. Qiu, *Energy Environ. Sci.*, 2016, **9**, 1299-1307.
15. Q. Cheng, C. Yang, K. Tao and L. Han, *Electrochim. Acta*, 2020, **341**, 136042.
16. K. Tao, X. Han, Q. Ma and L. Han, *Dalton Trans.*, 2018, **47**, 3496-3502.
17. S. Liu and S. C. Jun, *J. Power Sources*, 2017, **342**, 629-637.
18. L. Cheng, Y. Hu, L. Ling, D. Qiao, S. Cui and Z. Jiao, *Electrochim. Acta*, 2018, **283**, 664-675.
19. Y. Tian, Z. Xue, Q. Zhao, J. Guo, K. Tao and L. Han, *Dalton Trans.*, 2022, **51**, 4406-4413.
20. X. Zhang, Y. Tian, W. Lu, S. Yang, N. Qu, Q. Zhang, D. Lei and A. Liu, *Chemelectrochem*, 2021, **8**, 3629-3636.
21. M. Xu, H. Guo, T. Zhang, J. Zhang, X. Wang and W. Yang, *J. Energy Storage*, 2021, **35**, 102303.
22. Y. Shen, K. Zhang, B. Chen, F. Yang, K. Xu and X. Lu, *J. Colloid Interface Sci.*, 2019, **557**, 135-143.
23. K. Le, M. Gao, W. Liu, J. Liu, Z. Wang, F. Wang, V. Murugadoss, S. Wu, T. Ding and Z. Guo, *Electrochim. Acta*, 2019, **323**.
24. L. Li, Y. Ding, H. Huang, D. Yu, S. Zhang, H.-Y. Chen, S. Ramakrishna and S. Peng, *J. Colloid Interface Sci.*, 2019, **540**, 389-397.